MATER. RES. LETT.
2024, VOL. 12, NO. 4, 315–323
https://doi.org/10.1080/21663831.2024.2328375

ORIGINAL REPORTS

OPEN ACCESS Check for updates

Colossal negative thermal expansion over a wide temperature span in dynamically self-assembled MnCo(Ge,Si)/epoxy composites

Wenhui Guo[a], Xuefei Miao [a], Zhubing Yan[a], Yunlong Chen[a], Yong Gong[a], Fengjiao Qian[b], Feng Xu [a] and Luana Caron [c,d]

[a]School of Materials Science and Engineering, Nanjing University of Science and Technology, Nanjing, People's Republic of China; [b]College of Physics, Nanjing University of Aeronautics and Astronautics, Nanjing, People's Republic of China; [c]Department of Physics, Bielefeld University, Bielefeld, Germany; [d]Helmholtz-Zentrum Berlin für Materialien und Energie, Berlin, Germany

ABSTRACT

The achievement of significant negative thermal expansion (NTE) over a wide temperature range (ΔT_{NTE}) has posed a formidable challenge for NTE materials. In the present study, textured MnCo(Ge,Si)/epoxy composites were prepared by magnetic field-assisted dynamic self-assembly of multi-component $Mn_{0.945}Co_{1.055}Ge_{1-x}Si_x$ particles. The utilization of multi-component particles with tunable transition temperatures significantly amplifies the temperature range over which the NTE occurs, surpassing the limitations of conventional single-component composites. The textured microstructure enables the extension of lattice-level NTE to reach the macroscopic level, which is manifested by a remarkably large NTE coefficient of -328.7×10^{-6}/K between 288.2 and 431.1 K.

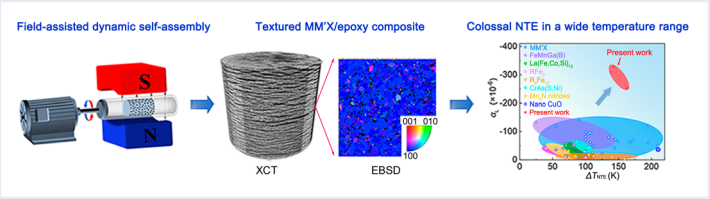

IMPACT STATEMENT

Colossal NTE with a coefficient α_L of -328.7×10^{-6}/K is achieved over a wide temperature range of 142.9 K between 288.2 and 431.1 K, representing the largest α_L among all reported NTE materials.

ARTICLE HISTORY
Received 3 January 2024

KEYWORDS
Magnetostructural transition; magnetocaloric alloy; negative thermal expansion; MM'X alloy

1. Introduction

Negative thermal expansion (NTE) materials are a fascinating group of materials that contract as their temperature increases, which is opposite from the typical positive thermal expansion (PTE) behavior exhibited by most materials. NTE materials can be incorporated with PTE materials to create composites that have zero or reduced thermal expansion, which is of crucial importance to a variety of technological applications, e.g. thermal stress management, high-precision engineering, thermal barrier coating and aerospace industry [1–4].

The origin of NTE can be attributed to various underlying mechanisms that make a negative contribution to the overall thermal expansion against anharmonic vibration of atoms. For instance, NTE has been observed in framework materials that are characterized by phonon-driven structural distortions or asymmetric vibration and rotation of structural units within the crystal lattice [5–10]. The NTE phenomenon can also be a macroscopic manifestation of the strong coupling between lattice, electron and spin degrees of freedom at the microscopic scale. The microscopic charge transfer in $BiNiO_3$ [11], local chemical ordering in PtNi nanoparticles [12], magneto-volume effect in magnetic alloys [4,13–20], and ferroelectric ordering in $PbTiO_3$-based compounds [21] also lead to a macroscopic NTE behavior. Apart from that, the abrupt increase in the unit-cell volume across the martensitic transition brings a giant/colossal NTE in the MM'X (M, M' = Mn, Fe, Co, Ni; X = Si, Ge) [22–26], Fe_3NiB_x [27] and $Fe_{44-x}Mn_{28}Ga_{28+x}$ [28,29] alloys.

Among the diverse classes of NTE materials, the MM'X family has attracted considerable attention due to their exceptionally large NTE. For example, the $(Mn_{0.95}Ni_{0.05})CoGe$ alloy shows an NTE coefficient (α_L)

CONTACT Xuefei Miao xuefeimiao@njust.edu.cn; Feng Xu xufeng@njust.edu.cn; Luana Caron luana.caron@uni-bielefeld.de

Supplemental data for this article can be accessed online at https://doi.org/10.1080/21663831.2024.2328375.

of about -207×10^{-6}/K [30], which is almost one order of magnitude larger than that of most NTE materials [1,2]. However, such a large NTE can only be obtained in a narrow temperature span (ΔT_{NTE}) of about 50 K [30]. The ΔT_{NTE} can be enlarged to $\sim$ 195 K by compositional variation in Fe-doped MnNiGe alloys, whereas this is realized at the expense of a significant reduction of the α_L [25]. Therefore, it has been a great challenge to achieve both large NTE and a wide temperature span for the MM'X materials.

One prominent feature of the MM'X materials is the anisotropic structural deformation close to the martensitic transition temperature (T_t). The orthorhombic lattice shrinks along the a_{Ort} axis by $\sim$10% upon heating, while it expands along the b_{Ort} and c_{Ort} axes by $\sim$7% and $\sim$0.4%, respectively [25,31]. As a result, a colossal NTE with a potential maximum α_L of $\sim 2000 \times 10^{-6}$/K may be developed in $<100>_{\mathrm{Ort}}$-textured MM'X materials, but the ΔT_{NTE} will still be limited by the sharp martensitic transition. In the present work, we successfully fabricated $<100>_{\mathrm{Ort}}$-textured MnCo(Ge,Si)/epoxy composites by dynamical self-assembly in a magnetic field [32–34]. In order to tackle with the narrow ΔT_{NTE}, multi-component $Mn_{0.945}Co_{1.055}Ge_{1-x}Si_x$ particles with variable T_ts were used in the composites, which yielded martensitic transitions in tandem over a wide temperature range and thus a significantly enlarged ΔT_{NTE}.

2. Materials and methods

Polycrystalline samples with nominal compositions of $Mn_{0.945}Co_{1.055}Ge_{1-x}Si_x$ (x = 0.09, 0.12, 0.15, 0.17, 0.19 and 0.21) were prepared by arc melting under high-purity argon atmosphere. The ingots were remelted four times to ensure compositional homogeneity and subsequently annealed at 1123 K for 4 days in evacuated quartz tubes before being quenched in water.

The annealed $Mn_{0.945}Co_{1.055}Ge_{1-x}Si_x$ ingots were pulverized through multiple thermal cycles in liquid nitrogen. The pulverized powders with diameters between 20 and 50 μm from 6 different compositions (i.e. x = 0.09, 0.12, 0.15, 0.17, 0.19 and 0.21) were mixed in an equal ratio and used for the subsequent dynamic self-assembly process (see the illustration in Figure 1). The multi-component design aims at enlarging the temperature span of the NTE since the lattice-level NTE appears only in a narrow temperature range around T_t for a single composition. The multi-component powders were then suspended in epoxy. The amount of epoxy was set to be 10, 12.5 and 15 wt.% with respect to the weight of the multi-component powders. The suspension after degassing in a vacuum was transferred into a cylindrical plastic mould that was subsequently rotated along its long axis at a speed of 30 r/min for 10 h. A static magnetic field of 1 T was applied perpendicular to the long axis of the mould during the rotation. Self-assembled multi-component $Mn_{0.945}Co_{1.055}Ge_{1-x}Si_x$/epoxy composites with a diameter of 5 mm and a length of 15 mm were finally obtained after curing at room temperature for 10 h.

A vibrating sample magnetometer (VSM, Lakeshore 7400s) and a differential scanning calorimeter (DSC, PerkinElmer DSC 6000) were employed to characterize the magnetic and structural transitions. In situ temperature-dependent X-ray diffraction (XRD) measurements were performed using a PANalytical Empyrean diffractometer with Cu-Kα radiation. The morphology and crystallographic orientation of the dynamically self-assembled multi-component composites were examined using a scanning electron microscope (SEM, JSM 7200F) equipped with electron backscatter diffraction (EBSD) detectors. The micro- and nano-scale structural analyses on the dynamically self-assembled composite were carried out using a transmission electron microscope (TEM, FEI Tecnai G2 F20). The linear thermal expansion ($\Delta L/L_0$) curves were measured by a thermal dilatometer (Linseis DIL L75 VS). Uniaxial compression tests were performed using a universal test machine (INSTRON 5982) with a strain rate of 1×10^{-4} s^{-1}.

3. Results and discussion

Figure 2(a) shows the temperature-dependent magnetization (M-T) curves, where a sharp paramagnetic-ferromagnetic (PM-FM) transition with noticeable thermal hysteresis (ΔT_{hys}) was observed in the x = 0.09 sample. Besides, the FM transition is accompanied by a strong endothermic or exothermic peak in the DSC curves (Figure 2(b)). This suggests the occurrence of a first-order magnetostructural transition, where the hexagonal-orthorhombic structural transition coincides with the PM-FM transition. According to the M-T and DSC curves, the T_t rises with increasing Si content from 0.09 to 0.17, while the magnetostructural transition is retained. In contrast, a different phase transition character is observed in the x = 0.19 and 0.21 samples. Although endothermic and exothermic peaks are still present in the DSC curves (Figure 2(b)), the x = 0.19 and 0.21 samples show a second-order FM transition with negligible ΔT_{hys} in the M-T curves (Figure 2(a)). This suggests the decoupling of the structural and magnetic transitions. Based on the magnetometry and calorimetry analyses, a magnetic and structural phase diagram has been constructed for the $Mn_{0.945}Co_{1.055}Ge_{1-x}Si_x$ series

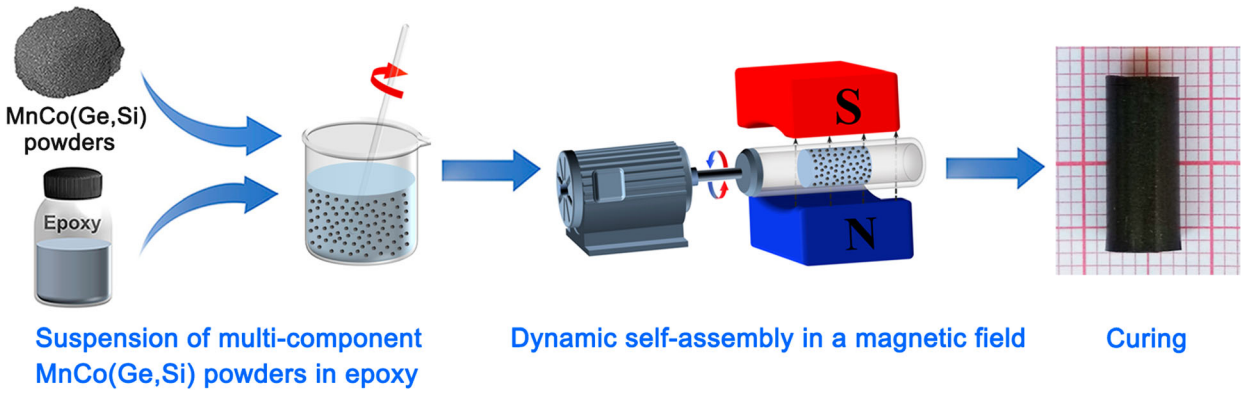

Figure 1. Schematics of the field-assisted self-assembly process.

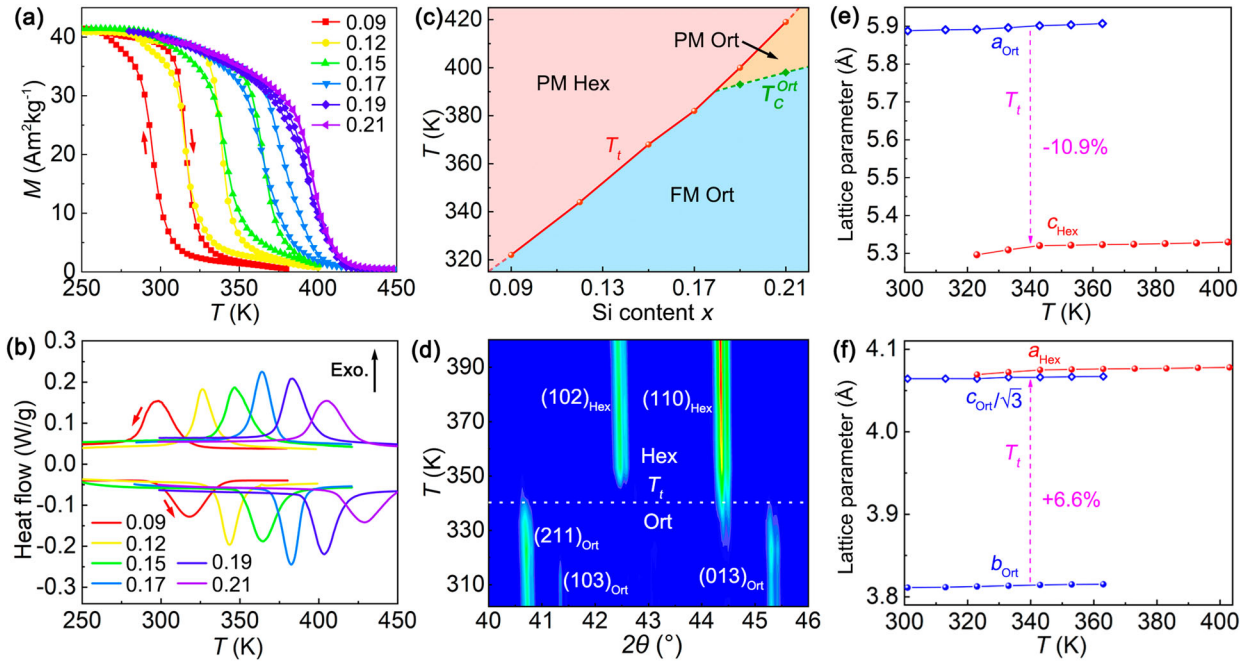

Figure 2. (a) *M-T* and (b) DSC curves, (c) magnetic and structural phase diagram of the $Mn_{0.945}Co_{1.055}Ge_{1-x}Si_x$ alloys. (d) Contour plot of temperature-dependent XRD patterns of the $x = 0.12$ sample. (e) and (f) Temperature-dependent lattice parameters of the $x = 0.12$ sample. The errors on lattice parameters are smaller than the symbol sizes.

of materials (see Figure 2(c)). According to the phase diagram, all of the samples are in the FM orthorhombic state at room temperature, which offers the potential to manipulate the orientation of the free powders using a magnetic field.

Figure 2(d) displays a contour plot of the XRD patterns from the $x = 0.12$ sample as an example. A structural transition from TiNiSi-type orthorhombic (space group *Pnma*) to Ni_2In-type hexagonal (space group $P6_3/mmc$) is detected at around 340 K, in agreement with the magnetometry and calorimetry results. Thermal evolution of the lattice parameters across the structural transition is derived from Rietveld refinement and displayed in Figure 2(e) and (f). Previous studies revealed that the lattice parameters of the orthorhombic and hexagonal phases are related by $a_{Ort} = c_{Hex}$, $b_{Ort} = a_{Hex}$, and $c_{Ort} = \sqrt{3}a_{Hex}$ due to the crystallographic relationship between the two phases. According to the XRD results in Figure 2(e), the orthorhombic lattice shrinks by 10.9% along the a_{Ort} axis upon heating, manifesting a remarkable NTE at the lattice level near the T_t. In contrast, the orthorhombic lattice expands by 6.6% and 0.4% along the b_{Ort} and c_{Ort} axes respectively, exhibiting normal PTE. Consequently, in order to take advantage of the large NTE along the a_{Ort}-axis, it is necessary to introduce a strong $<100>_{Ort}$ texture in the $Mn_{0.945}Co_{1.055}Ge_{1-x}Si_x$ materials.

Textured $Mn_{0.945}Co_{1.055}Ge_{1-x}Si_x$/epoxy composites have been successfully fabricated by field-assisted dynamic self-assembly of the ferromagnetic $Mn_{0.945}$

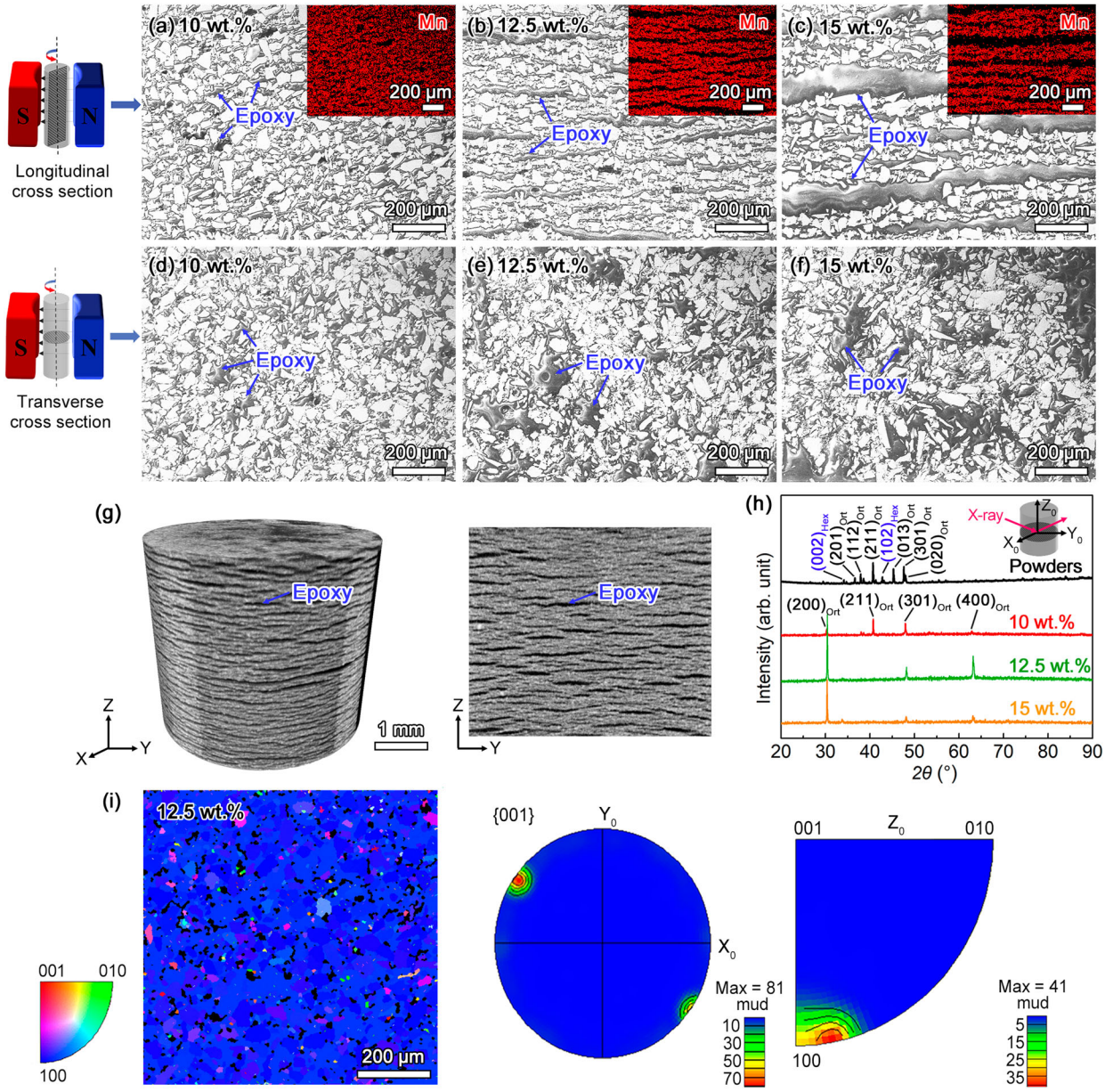

Figure 3. SEM images collected from (a-c) longitudinal and (b-f) transverse cross sections of dynamically self-assembled multi-component composites. The insets in (a), (b) and (c) are EDS mappings of the Mn element. (g) 3D and 2D XCT images of the multi-component composite with 12.5 wt.% epoxy. (h) XRD patterns collected from the multi-component powders and composites. (i) EBSD analysis of the transverse cross section of the multi-component composite with 12.5 wt.% epoxy.

$Co_{1.055}Ge_{1-x}Si_x$ powders (see details in the Materials and methods section). Figure 3(a)-(f) present images taken from the longitudinal and transverse cross sections of the composites. The microstructure of the composite with 10 wt.% epoxy is characterized by a uniform distribution of $Mn_{0.945}Co_{1.055}Ge_{1-x}Si_x$ powders in the epoxy matrix (Figure 3(a) and (b)). Interestingly, lamellar structure appears in the longitudinal cross section of the composite with 12.5 wt.% epoxy (Figure 3(b)), which is also visualized in the EDS (the inset of Figure 3(b)) and X-ray computed tomography (XCT) analyses (Figure 3(g)). This lamellar structure is ascribed to the complex interplay between magnetic force from the external magnetic field, dipole–dipole interaction between neighboring particles, viscous drag from the epoxy and centripetal force during the field-assisted self-assembly process [32–34]. The thickness of the epoxy layer increases as the epoxy content rises from 12.5 to 15 wt.% (Figure 3(c)).

XRD and EBSD analyses were performed to explore the grain orientation in the multi-component $Mn_{0.945}Co_{1.055}Ge_{1-x}Si_x$/epoxy composites. Figure 3(h) displays the XRD patterns collected from the multi-component powders and the transverse cross section of the dynamically self-assembled multi-component

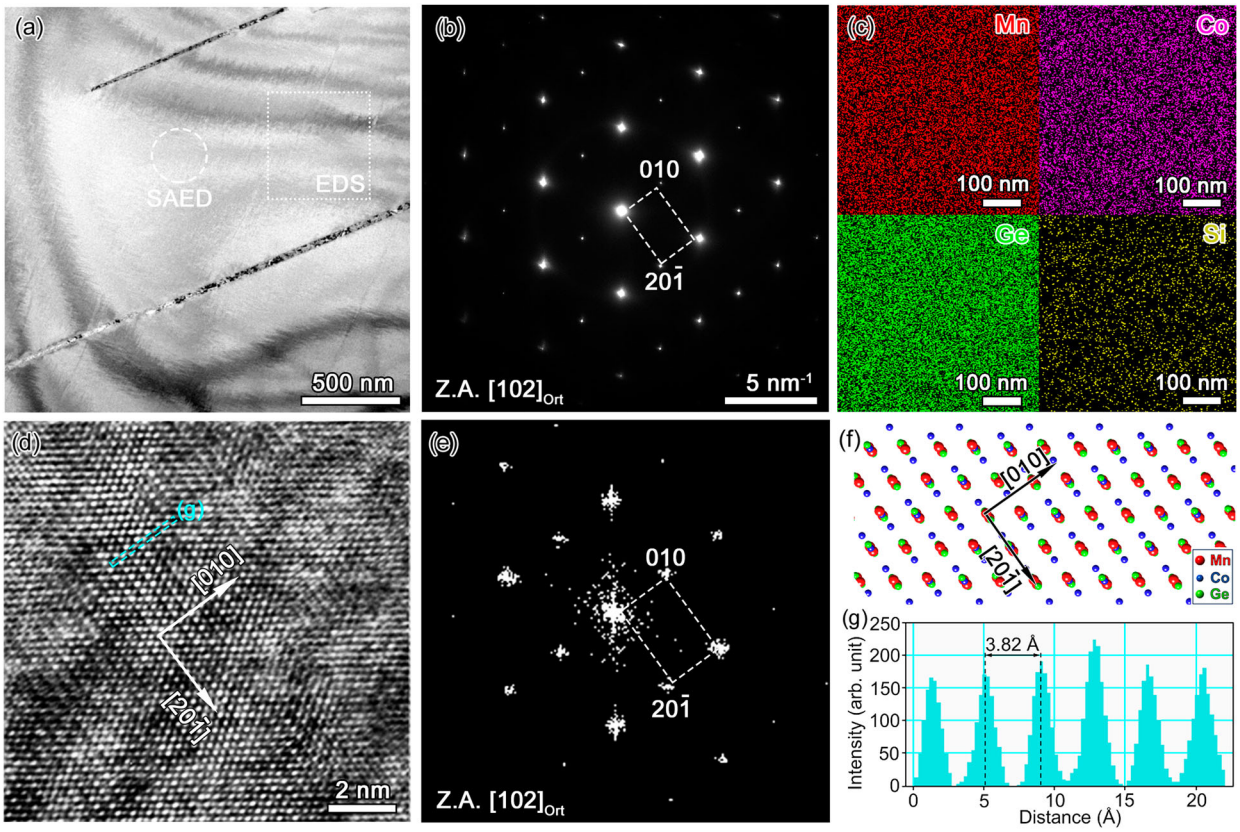

Figure 4. BF-TEM image and (b) SAED pattern taken from a specimen lift out from the dynamically self-assembled multi-component composite with 12.5 wt.% epoxy. (c) EDS maps of selected region in (a). (d) HRTEM image and (e) corresponding FFT of the region enclosed by solid lines in (a). (f) Schematic representation of the atomic configuration viewing along the $[102]_{Ort}$ direction. (g) Intensity profiles of the region enclosed by the dashed line in (d).

composites. The diffraction peaks of the powders can be mainly indexed by the TiNiSi-type orthorhombic phase. There are also a couple of weak reflections from the Ni_2In-type hexagonal phase, which is originated from the $Mn_{0.945}Co_{1.055}Ge_{0.91}Si_{0.09}$ particles showing a hexagonal-orthorhombic transition around room temperature (Figure 2 (a) and (b)). In contrast with the XRD pattern of the multi-component powders, the XRD patterns of the dynamically self-assembled composites with 12.5 and 15 wt.% epoxy are characterized by strong {H00}-type reflections (e.g. (200) and (400)), suggesting a strong $<100>_{Ort}$ texture along the long axis of cylindrical-shaped samples. Nevertheless, the preferred grain orientation is less significant in the composite with 10 wt.% epoxy, which may arise from the large constraints between neighbouring particles suspended in a limited amount of epoxy. Additionally, the preferred orientation of the $Mn_{0.945}Co_{1.055}Ge_{1-x}Si_x$ particles in the composites with 12.5 wt.% epoxy has also been verified by the EBSD orientation maps, pole figures and inverse pole figures in Figure 3(i).

Consequently, the XRD and EBSD results reveal a strong $<100>_{Ort}$ texture in the multi-component $Mn_{0.945}Co_{1.055}Ge_{1-x}Si_x$/epoxy composites with 12.5 and 15 wt.% epoxy. Our previous neutron diffraction experiments reveal that the magnetic moments in MnCoGe-based alloys are aligned along the *c*-axis of the orthorhombic structure [31]. As a result, $<001>_{Ort}$ texture was obtained by means of aligning the $Mn_{0.6}Fe_{0.4}NiGe_{0.5}Si_{0.5}$ particles in a static magnetic field [26]. In contrast, here we applied a magnetic field perpendicular to the rotation axis of the $Mn_{0.945}Co_{1.055}Ge_{1-x}Si_x$ particles (see Figure 1). Therefore, the particles are reoriented with the *c*-axis perpendicular to their rotation axis, leading to the desirable preferred orientation of $<100>_{Ort}$ parallel to the rotation axis (see Figure 3(g) and (h)).

Figure 4 shows the TEM observations on a thin specimen lifted out from the multi-component composite with 12.5 wt.% epoxy by focused ion beam (FIB). Thin and parallel laths can be observed in the bright-field (BF) TEM image in Figure 4(a), manifesting itself as the orthorhombic martensite, which has also been observed in other MM'X-type materials [35–38]. The TiNiSi-type orthorhombic structure is also confirmed by the selected area electron diffraction (SAED) pattern in Figure 4(b), which was taken from the $[102]_{Ort}$ zone axis (Z.A.).

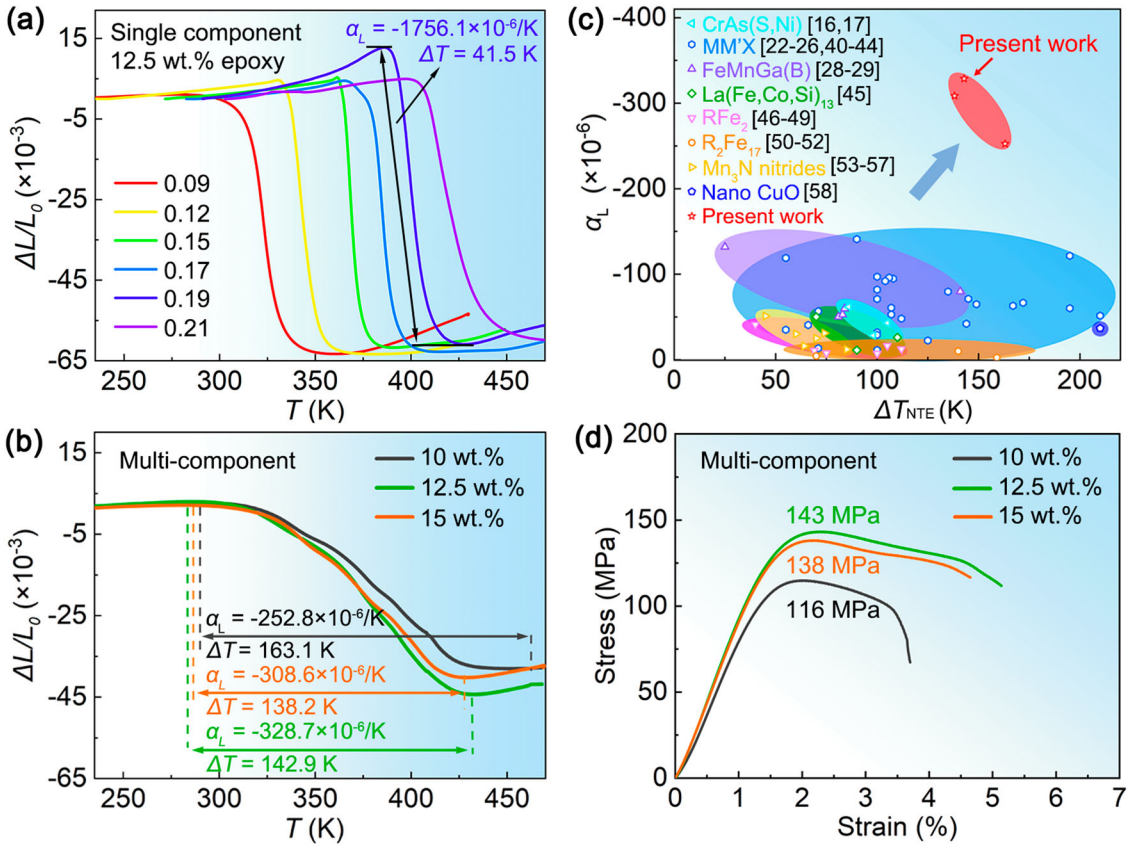

Figure 5. Temperature-dependent linear thermal expansion $\Delta L/L_0$ along the $<100>_{Ort}$ textured direction of the dynamically self-assembled (a) single-component and (b) multi-component $Mn_{0.945}Co_{1.055}Ge_{1-x}Si_x$/epoxy composites. (c) Ashby-like plot comparing the ΔT_{NTE} and α_L of different NTE magnetic materials [16,17,22–26,28,29,40–58]. (d) Compressive stress-strain curves for the dynamically self-assembled multi-component composites with the 10, 12.5 and 15 wt.% epoxy.

The EDS elemental maps (Figure 4(c)) reveal compositional homogeneity in the area enclosed by dotted lines in Figure 4(a). Figure 4(d) and (e) present a high-resolution TEM (HRTEM) image and a corresponding fast Fourier transform (FFT) pattern, respectively. The atomic arrangement along the $[010]_{Ort}$ and $[20\text{-}1]_{Ort}$ crystallographic directions can be unambiguously distinguished in the HRTEM image (see the schematic illustration in Figure 4(f)). Additionally, the lattice parameter b of the orthorhombic phase is estimated to be 3.82 Å by the periodicity of the intensity profile (see Figure 4(g)) along the $[010]_{Ort}$ direction, which is consistent with the neutron diffraction results and literature reports [31,39].

Figure 5(a) presents the temperature-dependent linear thermal expansion ($\Delta L/L_0$) along the long axis of the single-component $Mn_{0.945}Co_{1.055}Ge_{1-x}Si_x$/epoxy composites. A large NTE coefficient (α_L) of about -1756.1×10^{-6}/K is realized in the single-component composites due to the martensitic transition. This is the largest reported magnitude of α_L among NTE materials. However, the temperature span of the NTE is less than 50 K in the single-component composites due to the relatively sharp martensitic transition (see Figure 2). The narrow ΔT_{NTE} has been a common issue for metallic materials whose NTE property is induced by martensitic phase transitions [1]. In strong contrast to the narrow ΔT_{NTE} in single-component composites, a wide ΔT_{NTE} up to 163.1 K is obtained in the multi-component composites that contain $Mn_{0.945}Co_{1.055}Ge_{1-x}Si_x$ particles from six different compositions and 10 wt.% epoxy. The design of multi-components takes advantage of the martensitic transition from each composition and results in consecutive martensitic transitions over a wide temperature range. Besides, both α_L and ΔT_{NTE} are influenced by the amount of epoxy. The magnitude of α_L increases from 252.8×10^{-6}/K to 328.7×10^{-6}/K as the amount of epoxy rises from 10 to 12.5 wt.%, while it shows a decrease with further increase in the amount of epoxy to 15 wt.%. The non-monotonic change in α_L with respect to the amount of epoxy can be attributed to the competition between crystallographic texture and PTE of epoxy itself. As shown in Figure 3(h), the $<001>_{Ort}$ orientation of the $Mn_{0.945}Co_{1.055}Ge_{1-x}Si_x$ powders is enhanced with an increase in the epoxy content from 10 to 12.5 wt.% due to the improved mobility of the $Mn_{0.945}Co_{1.055}Ge_{1-x}Si_x$ powders during the

field-assisted self-assembly process. As a result, stronger NTE is observed in the composites with 12.5 wt.% epoxy as compared to that with 10 wt.% epoxy. Nevertheless, the NTE of the composite is weakened with a further increase in the epoxy content to 15 wt.%, which is ascribed to the increased contribution of epoxy with PTE. The Ashby-like plot in Figure 5(c) compares the ΔT_{NTE} and α_L for various NTE magnetic materials. A combination of colossal NTE and a large temperature span makes the dynamically self-assembled multi-component $Mn_{0.945}Co_{1.055}Ge_{1-x}Si_x$/epoxy composites highly competitive among all reported NTE magnetic materials [16,17,22–26,28,29,40–58]. It is worth noting that the wide variety of compounds within the MM'X family provides the flexibility to adjust the T_t across a wide temperature range. This capability opens up the potential for further expanding the ΔT_{NTE}.

Additionally, mechanical properties are also critical for practical applications of NTE materials. The compressive stress–strain curves of the dynamically self-assembled multi-component $Mn_{0.945}Co_{1.055}Ge_{1-x}Si_x$/epoxy composites are shown in Figure 5(d). It can be found that the composite with 12.5 wt.% epoxy exhibits a maximum compressive stress of 143 MPa, remarkably higher than the Ag-epoxy-bonded $MnCoGe_{0.99}In_{0.01}$ (70.4 MPa) [22] and In-bonded $Mn_{0.6}Fe_{0.4}NiGe_{0.5}Si_{0.5}$ (48 MPa) [26] composites.

4. Conclusions

In summary, this work demonstrates a new strategy to achieve both a large NTE coefficient and a wide temperature range for MM'X materials. This is realized by dynamic self-assembly of multi-component $Mn_{0.945}Co_{1.055}Ge_{1-x}Si_x$/epoxy composites in a magnetic field, which leads to a preferred $<100>_{Ort}$ orientation for the $Mn_{0.945}Co_{1.055}Ge_{1-x}Si_x$ particles. The colossal NTE along the a_{Ort} axis of the orthorhombic lattice across the martensitic transition manifests in the macroscopic level due to the strong $<100>_{Ort}$ texture. As a result, a linear NTE coefficient of -328.7×10^{-6}/K has been obtained in the dynamically self-assembled multi-component MM'X/epoxy composites, which represents one of the highest α_L values among all reported NTE materials. Furthermore, the integration of multi-component $Mn_{0.945}Co_{1.055}Ge_{1-x}Si_x$ particles with gradually varying martensitic transition temperatures substantially broadens the NTE temperature range, achieving an impressive ΔT_{NTE} of 142.9 K between 288.2 and 431.1 K. Consequently, the remarkable synergy between colossal NTE and a wide temperature span makes the dynamically self-assembled multi-component MM'X/epoxy composites highly competitive within the realm of NTE materials.

Acknowledgements

This work was carried out in the framework of the Joint Lab BiBer.

Disclosure statement

No potential conflict of interest was reported by the author(s).

Funding

This work was supported by the National Natural Science Foundation of China [grant numbers 12004179, U1832191, 51801102, 52371189]; the Natural Science Foundation of Jiangsu Province [grant number BK20231458]; the Fundamental Research Funds for the Central Universities [grant number 30922010802]; the Sino-German Mobility Program from the Sino-German Center for Research Promotion (SGC) [grant number M-0447].

ORCID

Xuefei Miao http://orcid.org/0000-0003-4930-9108
Feng Xu http://orcid.org/0000-0001-5802-7925
Luana Caron http://orcid.org/0000-0002-2291-9814

References

[1] Song Y, Shi N, Deng S, et al. Negative thermal expansion in magnetic materials. Prog Mater Sci. 2021;121:100835. doi:10.1016/j.pmatsci.2021.100835
[2] Shi N, Song Y, Xing X, et al. Negative thermal expansion in framework structure materials. Coord Chem Rev. 2021;449:214204. doi:10.1016/j.ccr.2021.214204
[3] Zhang Y, Chen B, Guan D, et al. Thermal-expansion offset for high-performance fuel cell cathodes. Nature. 2021;591:246–251. doi:10.1038/s41586-021-03264-1
[4] Hu Q, Wang J, Yan Y, et al. Anomalous thermal expansion in the deep super-cooled liquid region of a ZrCuAlAg bulk metallic glass. Mater Res Lett. 2017;6:121–129. doi:10.1080/21663831.2017.1408713
[5] Schneider C, Bodesheim D, Ehrenreich MG, et al. Tuning the negative thermal expansion behavior of the metal-organic framework Cu_3BTC_2 by fetrofitting. J Am Chem Soc. 2019;141:10504–10509. doi:10.1021/jacs.9b04755
[6] Attfield JP. A fresh twist on shrinking materials. Nature. 2011;480:465–466. doi:10.1038/480465a
[7] Goodwin AL, Calleja M, Conterio MJ, et al. Colossal positive and negative thermal expansion in the framework material $Ag_3[Co(CN)_6]$. Science. 2008;319:794–797. doi:10.1126/science.1151442
[8] Mary TA, Evans JSO, Vogt T, et al. Negative thermal expansion from 0.3 to 1050 Kelvin in ZrW_2O_8. Science. 1996;272:90–92. doi:10.1126/science.272.5258.90
[9] Das D, Jacobs T, Barbour LJ. Exceptionally large positive and negative anisotropic thermal expansion of an organic crystalline material. Nat Mater. 2010;9:36–39. doi:10.1038/nmat2583

[10] Sanson A. On the switching between negative and positive thermal expansion in framework materials. Mater Res Lett. 2019;7:412–417. doi:10.1080/21663831.2019.1621957
[11] Azuma M, Chen WT, Seki H, et al. Colossal negative thermal expansion in $BiNiO_3$ induced by intermetallic charge transfer. Nat Commun. 2011;2:347. doi:10.1038/ncomms1361
[12] Li Q, Zhu H, Zheng L, et al. Local chemical ordering and negative thermal expansion in PtNi alloy nanoparticles. Nano Lett. 2017;17:7892–7896. doi:10.1021/acs.nanolett.7b04219
[13] Mohn P. A century of zero expansion. Nature. 1999;400:18–19. doi:10.1038/21778
[14] Yuan X, Sun Y, Guo H, et al. Design of negative/nearly zero thermal expansion behavior over a wide temperature range by multi-phase composite. Mater Des. 2021;203:109501. doi:10.1016/j.matdes.2021.109591
[15] Lu H, Sun Y, Shi K, et al. Effects of Fe doping on structure, negative thermal expansion, and magnetic properties of antiperovskite Mn_3GaN compounds. J Am Ceram Soc. 2023;106:3792–3799. doi:10.1111/jace.19031
[16] Hu Y, Zheng X, Ma G, et al. Giant negative thermal expansion in antiferromagnetic CrAs-based compounds. Phys Rev Appl. 2019;12:034027. doi:10.1103/PhysRevApplied.12.034027
[17] Suzuki T, Ido H. Spontaneous magnetostriction of $CrAs_{1-x}S_x$ compounds. J Magn Magn Mater. 1995;140:149–150. doi:10.1016/0304-8853(94)01047-1
[18] Yu C, Lin K, Cao Y, et al. Two-dimensional zero thermal expansion in low-cost $Mn_xFe_{5-x}Si_3$ alloys via integrating crystallographic texture and magneto-volume effect. Sci China Mater. 2022;65:1912–1919. doi:10.1007/s40843-021-1996-2
[19] Cen D, Wang B, Chu R, et al. Design of (Hf,Ta)Fe_2/Fe composite with zero thermal expansion covering room temperature. Scr Mater. 2020;186:331–335. doi:10.1016/j.scriptamat.2020.05.048
[20] Rao Z, Tung PY, Xie R, et al. Machine learning-enabled high-entropy alloy discovery. Science. 2022;378:78–85. doi:10.1126/science.abo4940
[21] Chen J, Fan L, Ren Y, et al. Unusual transformation from strong negative to positive thermal expansion in $PbTiO_3$-$BiFeO_3$ perovskite. Phys Rev Lett. 2013;110:115901. doi:10.1103/PhysRevLett.110.115901
[22] Zhao Y, Hu F, Bao L, et al. Giant negative thermal expansion in bonded MnCoGe-based compounds with Ni_2In-type hexagonal structure. J Am Chem Soc. 2015;137:1746–1749. doi:10.1021/ja510693a
[23] Lin J, Tong P, Zhang K, et al. Colossal negative thermal expansion with an extended temperature interval covering room temperature in fine-powdered $Mn_{0.98}$CoGe. Appl Phys Lett. 2016;109:241903. doi:10.1063/1.4972234
[24] Zhao W, Sun Y, Liu Y, et al. Negative thermal expansion over a wide temperature range in Fe-doped MnNiGe composites. Front Chem. 2018;6:15. doi:10.3389/fchem.2018.00015
[25] Shen F, Zhou H, Hu F, et al. Cone-spiral magnetic ordering dominated lattice distortion and giant negative thermal expansion in Fe-doped MnNiGe compounds. Mater Horiz. 2020;7:804–810. doi:10.1039/C9MH01602C
[26] Zhou H, Tao K, Chen B, et al. Low-melting metal bonded MM′X/In composite with largely enhanced mechanical property and anisotropic negative thermal expansion. Acta Mater. 2022;229:117830. doi:10.1016/j.actamat.2022.117830
[27] Cui J, Sun Y, Yuan X, et al. Discovery of negative thermal expansion with giant thermal hysteresis in Fe_3NiB_x. Scr Mater. 2020;183:149–152. doi:10.1016/j.scriptamat.2020.03.035
[28] Sun XM, Cong DY, Ren Y, et al. Giant negative thermal expansion in Fe-Mn-Ga magnetic shape memory alloys. Appl Phys Lett. 2018;113:041903. doi:10.1063/1.5038860
[29] Sun XM, Cong DY, Ren Y, et al. Enhanced negative thermal expansion of boron-doped $Fe_{43}Mn_{28}Ga_{28.97}B_{0.03}$ alloy. J Alloys Compd. 2021;857:157572. doi:10.1016/j.jallcom.2020.157572
[30] Ren Q, Hutchison W, Wang J, et al. Negative thermal expansion of Ni-doped MnCoGe at room-temperature magnetic tuning. ACS Appl Mater Interfaces. 2019;11:17531–17538. doi:10.1021/acsami.9b02772
[31] Miao X, Gong Y, Caron L, et al. Switching the magnetostructural coupling in MnCoGe-based magnetocaloric materials. Phys Rev Mater. 2020;4:104407. doi:10.1103/PhysRevMaterials.4.104407
[32] Grzybowski BA, Stone HA, Whitesides GM. Dynamic self-assembly of magnetized, millimetre-sized objects rotating at a liquid-air interface. Nature. 2000;405:1033–1036. doi:10.1038/35016528
[33] Grzybowski BA, Wiles JA, Whitesides GM. Dynamic self-assembly of rings of charged metallic spheres. Phys Rev Lett. 2003;90:083903. doi:10.1103/PhysRevLett.90.083903
[34] Gizynski K, Lee T, Grzybowski BA. Dynamic self-assembly of magnetic/polymer composites in rotating frames of reference. Adv Mater. 2017;29:1700614. doi:10.1002/adma.201700614
[35] Li Y, Zeng Q, Wei Z, et al. An efficient scheme to tailor the magnetostructural transitions by staged quenching and cyclical ageing in hexagonal martensitic alloys. Acta Mater. 2019;174:289–299. doi:10.1016/j.actamat.2019.05.042
[36] Zhang T, Gong Y, Wang B, et al. Crystallography of the martensitic transformation between Ni_2In-type hexagonal and TiNiSi-type orthorhombic phases. J Mater Sci Technol. 2022;104:59–66. doi:10.1016/j.jmst.2021.06.051
[37] Ma SC, Ge Q, Yang S, et al. Investigation of the martensitic microstructure and magnetostructural coupling in rapidly solidified Mn-Ni-Fe-Ge rod samples. J Alloys Compd. 2017;729:1190–1194.
[38] Ma S, Ge Q, Han X, et al. Magnetostructural transformation and magnetocaloric effect in rod-shaped Mn-Ni-Fe-Ge compounds by spraying casting. J Alloys Compd. 2018;742:648–655. doi:10.1016/j.jallcom.2018.01.339
[39] Ren Q, Hutchison WD, Wang J, et al. Magnetic and structural transitions tuned through valence electron concentration in magnetocaloric $MnCo_{1-x}Ni_xGe$. Chem Mater. 2018;30:1324–1334. doi:10.1021/acs.chemmater.7b04970
[40] Hao X, Hu Q, Gao M, et al. Giant negative thermal expansion in a textured MnCoSi alloy. J Alloys Compd. 2021;891:161915. doi:10.1016/j.jallcom.2021.161915

[41] Yang S, Ma S, Liu K, et al. Controllable negative thermal expansion by mechanical pulverizing in hexagonal $Mn_{0.965}Co_{1.035}Ge$ compounds. Inorg Chem. 2018;57:14199–14207. doi:10.1021/acs.inorgchem.8b02195
[42] Xu K, Li Z, Liu E, et al. Magnetocaloric effect and negative thermal expansion in hexagonal Fe doped MnNiGe compounds with a magnetoelastic AFM-FM-like transition. Sci Rep. 2017;7:41675. doi:10.1038/srep41675
[43] Zhu F, Lin J, Zhang X, et al. Giant antiferromagnetic negative thermal expansion in $(MnNiGe)_{1-x}(MnCoSn)_x$ compounds. J Alloys Compd. 2019;782:881–886. doi:10.1016/j.jallcom.2018.12.127
[44] Zhu F, Ji C, Lin J, et al. Large and antiferromagnetic negative thermal expansion over a wide temperature zone in $MnNiGe_{1-x}Pb_x$ ($0.04 \leq x \leq 0.2$) alloys. J Alloys Compd. 2020;820:153151. doi:10.1016/j.jallcom.2019.153151
[45] Huang R, Liu Y, Fan W, et al. Giant negative thermal expansion in $NaZn_{13}$-type $La(Fe,Si,Co)_{13}$ compounds. J Am Chem Soc. 2013;135:11469–11472. doi:10.1021/ja405161z
[46] Song Y, Chen J, Liu X, et al. Structure, magnetism, and tunable negative thermal expansion in $(Hf,Nb)Fe_2$ alloys. Chem Mater. 2017;29:7078–7082. doi:10.1021/acs.chemmater.7b02563
[47] Li B, Luo X, Wang H, et al. Colossal negative thermal expansion induced by magnetic phase competition on frustrated lattices in Laves phase compound $(Hf,Ta)Fe_2$. Phys Rev B. 2016;93:224405. doi:10.1103/PhysRevB.93.224405
[48] Li L, Tong P, Zou Y, et al. Good comprehensive performance of Laves phase $Hf_{1-x}Ta_xFe_2$ as negative thermal expansion materials. Acta Mater. 2018;161:258–265. doi:10.1016/j.actamat.2018.09.029
[49] Song Y, Sun Q, Xu M, et al. Negative thermal expansion in $(Sc,Ti)Fe_2$ induced by an unconventional magnetovolume effect. Mater Horiz. 2020;7:275–281. doi:10.1039/C9MH01025D
[50] Dan S, Mukherjee S, Mazumdar C, et al. Zero thermal expansion with high Curie temperature in $Ho_2Fe_{16}Cr$ alloy. RSC Adv. 2016;6:94809–94814. doi:10.1039/C6RA20216K
[51] Hao Y, Zhang X, Wang B, et al. Anomalous thermal expansion and magnetic properties of $Tm_2Fe_{17-x}Cr_x$ compounds. J Appl Phys. 2010;108:023915. doi:10.1063/1.3456444
[52] Hao Y, Liang F, Zhang X, et al. Thermal expansion anomaly and spontaneous magnetostriction of Gd_2Fe_{17} compound. J Rare Earths. 2011;29:772–775. doi:10.1016/S1002-0721(10)60540-6
[53] Hamada T, Takenaka K. Giant negative thermal expansion in antiperovskite manganese nitrides. J Appl Phys. 2011;109:07E–309. doi:10.1063/1.3540604
[54] Takenaka K, Takagi H. Giant negative thermal expansion in Ge-doped anti-perovskite manganese nitrides. Appl Phys Lett. 2005;87:261902. doi:10.1063/1.2147726
[55] Sun Y, Wang C, Wen Y, et al. Lattice contraction and magnetic and electronic transport properties of $Mn_3Zn_{1-x}Ge_xN$. Appl Phys Lett. 2007;91:231913. doi:10.1063/1.2822813
[56] Guo X, Lin J, Tong P, et al. Magnetically driven negative thermal expansion in antiperovskite $Ga_{1-x}Mn_xN_{0.8}Mn_3$ ($0.1 \leq x \leq 0.3$). Appl Phys Lett. 2015;107:202406. doi:10.1063/1.4936239
[57] Huang R, Li L, Cai F, et al. Low-temperature negative thermal expansion of the antiperovskite manganese nitride Mn_3CuN codoped with Ge and Si. Appl Phys Lett. 2008;93:081902. doi:10.1063/1.2970998
[58] Zheng X, Kubozono H, Yamada H, et al. Giant negative thermal expansion in magnetic nanocrystals. Nat Nanotechnol. 2008;3:724–726. doi:10.1038/nnano.2008.309